

Article

# Sacrificial Zinc Oxide Strategy-Enhanced Mesoporosity in MIL-53-Derived Iron–Carbon Composite for Methylene Blue Adsorption

Sander Dekyvere <sup>1,2,†</sup> , Mohamed Elhousseini Hilal <sup>1,2,3,†</sup> , Somboon Chaemchuen <sup>1,2</sup> , Serge Zhuiykov <sup>4</sup> and Francis Verpoort <sup>1,2,5,\*</sup> 

<sup>1</sup> State Key Laboratory of Advanced Technology for Materials Synthesis and Processing, Wuhan University of Technology, Wuhan 430070, China; sander4a@hotmail.com (S.D.); melhousseinihilal@hkcoche.org (M.E.H.); sama\_che@hotmail.com (S.C.)

<sup>2</sup> School of Materials Science and Engineering, Wuhan University of Technology, Wuhan 430070, China

<sup>3</sup> Hong Kong Centre for Cerebro-Cardiovascular Health Engineering (COCHE), Building 17W, Hong Kong Science Park, Hong Kong 999077, China

<sup>4</sup> Department of Solid State Science, Faculty of Science, Ghent University Global Campus, Songdo, 119 Songdomunhwa-Ro, Yeonsu-Gu, Incheon 404-840, Korea; serge.zhuiykov@ghent.ac.kr

<sup>5</sup> National Research Tomsk Polytechnic University, Lenin Avenue 30, 634034 Tomsk, Russia

\* Correspondence: francis@whut.edu.cn

† These authors contributed equally to this work.

**Abstract:** MOF-derived carbon-based materials have attracted widespread attention due to their relatively large surface area, morphology, and their stability in water. Considering these advantages, these materials present themselves as excellent adsorbents. In this work, a novel method was designed for the fabrication of a nano zero-valent-iron (nZVI) carbon composite. The utilization of zinc oxide nanorods (ZnONRs) in the role of sacrificial consumable nuclei for the synthesis of MIL-53 sacrificial zinc oxide nanorods (MIL-53-SNR) and the subsequent pyrolysis at 700 °C in the inert atmosphere led to a graphitic-supported nZVI material (Fe-C-SNR). Fe-C-SNR was compared with a commercial zinc oxide bulk (MIL-53-SB) and with a pristine MIL-53. By virtue of the ZnONRs, Fe-C-SNR exhibited a greatly improved mesoporous structure. Consequently, the pyrolyzed materials were applied as adsorbents for methylene blue. Fe-C-SNR's performance increased to more than double of the pyrolyzed MIL-53 (Fe-C), with a remarkably fast adsorption time (10 min) for a concentration of 10 mg L<sup>-1</sup> with only 200 mg L<sup>-1</sup> adsorbent required. This functional composite also displayed exceptional recyclability; after ten complete cycles, Fe-C-SNR was still capable of completely adsorbing the methylene blue. The utilization of ZnONRs proves itself advantageous and could further be extended to other MOFs for a wide range of applications.

**Keywords:** mesoporous material; zero-valent-iron nanoparticles; methylene blue adsorption; metal–organic framework



**Citation:** Dekyvere, S.; Hilal, M.E.; Chaemchuen, S.; Zhuiykov, S.; Verpoort, F. Sacrificial Zinc Oxide Strategy-Enhanced Mesoporosity in MIL-53-Derived Iron–Carbon Composite for Methylene Blue Adsorption. *Inorganics* **2022**, *10*, 59. <https://doi.org/10.3390/inorganics10050059>

Academic Editor: Roberto Nisticò

Received: 2 April 2022

Accepted: 22 April 2022

Published: 25 April 2022

**Publisher's Note:** MDPI stays neutral with regard to jurisdictional claims in published maps and institutional affiliations.



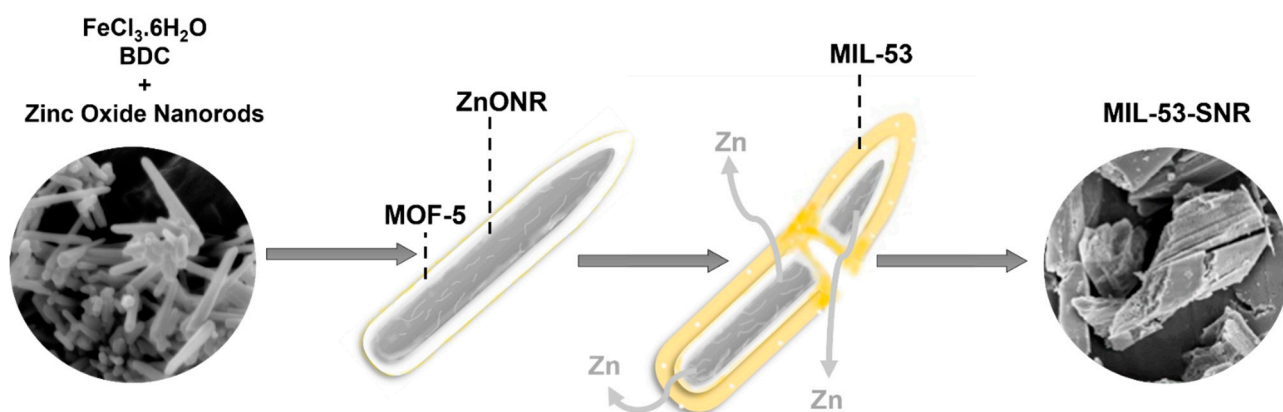
**Copyright:** © 2022 by the authors. Licensee MDPI, Basel, Switzerland. This article is an open access article distributed under the terms and conditions of the Creative Commons Attribution (CC BY) license (<https://creativecommons.org/licenses/by/4.0/>).

## 1. Introduction

Clean water is an indisputable necessity for humanity and the ever-increasing pollutant levels present threats to human health and our environment. Dye-containing wastewaters are some of the main contributors to the pollution of natural water, as they are toxic, carcinogenic, and are not biodegradable [1]. The primary sources of dye-containing wastewater are industrial sectors such as textile, pharmaceutical, food, mining, paper, printing, and leather industries. Of the main three categories of dyes, cationic dyes are of particular interest. Specifically, methylene blue (MB) is stable under light and heat and is difficult to biodegrade because of its complex structure [2]. Thus, developing effective and economical methods for removing MB dye from wastewater is a necessity. Many treatment techniques have been studied over the previous decades, such as photodegradation, biological and

chemical degradation, chemical and physical adsorption, and combinations of these treatments [3]. Among these methods, adsorption shows many practical advantages, such as low cost, facile operation, and quick removal [4]. A wide variety of adsorbents have been applied to remove dyes. Conventional porous materials that have been widely studied include zeolites, metal oxide nanoparticles, and activated carbons [5]. However, all these materials are associated with similar drawbacks, including their low surface area and recyclability. Over the last few years, zero-valent-iron nanoparticles (nZVI) have gained increasing interest in wastewater treatment due to their large surface area, small particle size, high dispersibility in water, and magnetic separation [6–11]. The main challenge for the practical application of nZVIs is the synthesis and preservation of the material. nZVIs are readily oxidized in the presence of other oxidants, ref. [12], forming oxide layers on the surface of the nZVI, which unavoidably reduces their practical performance for this application [13]. Therefore, porous materials such as bentonite [14], chitosan [15], diatomite [16], kaolinite [17], polyphenols [18], resin [19], sepiolite [20], and activated carbon [21] have been used to support or modify nZVIs to prevent agglomeration and oxidation. This approach is widely regarded as an efficient and facile pathway, as the  $\text{Fe}^0$  particles become more stable and the surface area and density of the functional groups can be increased [22,23]. Porous carbons are particularly regarded as exceptional hosts for nZVIs, endowing an enhanced surface area, highly mesoporous structure, good adsorption capacity, and providing the necessary protection from excessive detrimental surface oxidations [24–26]. Therefore, they present a higher activity, stability, and mobility towards removing various pollutants in wastewater compared to bare nZVIs. The composite of iron–carbon can be synthesized with generally facile methods using iron salts and porous carbon [27]. Even so, the dispersion and loading content of  $\text{Fe}^0$  would still need to be improved [28]. In this context, metal–organic frameworks (MOFs) are materials constructed by organic ligands and metal clusters. Recently, they have been utilized as precursors for the synthesis of metal/carbon composites, which provides the needed loading and dispersion for  $\text{Fe}^0$ . Iron–carbon composites have been obtained by the pyrolysis of Fe-MOFs, e.g., MIL-53, by adjusting the temperature depending on the required iron phase [23,29,30]. However, the challenge of creating suitable pore sizes in the carbonized material remains.

This work reports a novel strategy for fabricating an iron–carbon-based mesoporous material derived from an iron-containing MOF. The first stage, represented in Scheme 1, is a modified synthesis of MIL-53 using zinc oxide nanorods as sacrificial nuclei named ‘MIL-53-SNR’. The terephthalic acid binds with the outer surface of the ZnO, thereby etching zinc metal from the zinc oxide nanorods to form a MOF-5 layer. Simultaneously, the Zn in the MOF-5 is replaced by Fe, which synthesizes MIL-53. During these processes, the zinc gradually diffuses outward of the nuclei and thereby creates a highly defective MIL-53-SNR structure. The second step is the pyrolysis of the material under a nitrogen atmosphere at 700 °C. The as-prepared novel material iron–carbon sacrificial zinc oxide nanorods ‘Fe-C-SNR’ are characterized by XRD, FT-IR, SEM, and BET. A Fe-C-SNR is used as an adsorbent for methylene blue, displaying an excellent maximum adsorption capacity of 257  $\text{mg g}^{-1}$  compared to the maximum of 125  $\text{mg g}^{-1}$  by iron–carbon ‘Fe-C’ synthesized by the pyrolysis of a pristine MIL-53. To further assess the effect of the ZnO nanorods on performance, the third sample, iron–carbon sacrificial ZnO bulk ‘Fe-C-SB’, was prepared to evaluate the relationship between the ZnO morphology and the MB adsorption.



**Scheme 1.** Graphical representation of the sacrificial utilization of zinc oxide nanorods during the synthesis of MIL-53-SNR.

## 2. Results and Discussion

### 2.1. Characterizations

In this study, ZnO bulk and ZnONRs were implemented in the synthesis process to modify MIL-53. Commercial ZnO bulk possesses agglomerated particles of a few hundred micrometers in each direction. Scanning electron microscopy (SEM) was performed on as-synthesized zinc oxide nanorods, as illustrated in Figure S1. The nanorods displayed a smooth surface with an average length of 650 nm and a width of 60 nm; the XRD pattern is depicted in Figure S2. The X-ray diffraction patterns of MIL-53, MIL-53-SB, and MIL-53-SNR are displayed in Figure 1a and Figure S3; the peaks at  $9.2^\circ$ ,  $9.7^\circ$ ,  $12.6^\circ$ ,  $17.6^\circ$ ,  $18.6^\circ$ ,  $18.8^\circ$ , and  $25.4^\circ$  were present in all three samples. The doublet peak at  $9.2^\circ$  and  $9.7^\circ$  corresponds to the crystalline plane (001) of MIL-53. The peaks at  $12.6^\circ$  and  $25.4^\circ$  are assigned to the (100) and (010) crystal planes. These results confirm the successful synthesis of MIL-53 in all three samples [31,32]. Furthermore, the peaks at  $17.6^\circ$ ,  $18.6^\circ$ , and  $18.8^\circ$  match with the reported XRD patterns for MIL-53 [31,32]. The relatively small peak at  $21.9^\circ$ , present in MIL-53 and MIL-53-SB, is ascribed to the formation of MIL-88-B, which is synthesized through a similar procedure as MIL-53 but with some minor adaptations [33–35]. However, MIL-88-B can be a side product during the MIL-53 synthesis [36]. It has been reported that MIL-53 forms through homogenous nucleation and MIL-88-B forms through heterogeneous nucleation [34,35]; however, the peak matching with MIL-88-B was absent in the XRD pattern of MIL-53-SNR, which indicates that no heterogeneous nucleation occurred during the synthesis [34,35]. This difference between the zinc oxide bulk and the zinc oxide nanorods is attributed to the smaller size of the nanorods, which are quickly etched compared to the zinc oxide bulk. The successful preparation of MIL-53 was further confirmed by Fourier Transform Infrared (FTIR). The FTIR spectra of MIL-53, MIL-53-SB, and MIL-53-SNR are shown in Figure 1b. The broad peaks around  $3300\text{ cm}^{-1}$  are ascribed to the -OH stretching vibrations of the water molecules adsorbed on the surface [37]. The absorption peaks in the region of  $1400\text{--}1700\text{ cm}^{-1}$  exhibit the typical vibrational bands of the carboxylic acid function from the 1,4-BDC ligand [31,37]. A couple of sharp peaks around  $1540\text{ cm}^{-1}$  and  $1390\text{ cm}^{-1}$ , present in all three samples, correspond to the carboxyl groups' asymmetric and symmetric vibrations [37,38]. Typically, pure 1,4-BDC shows a peak at  $1693\text{ cm}^{-1}$ ; however, none of the samples exhibited this peak, confirming the absence of free BDC molecules. Instead, the band at  $530\text{ cm}^{-1}$  represents the metal-oxo bound between the carboxylic group of BDC and Fe [31]. These results further confirm the successful formation of MIL-53 in all three samples. The remaining peaks at  $750\text{ cm}^{-1}$ ,  $1665\text{ cm}^{-1}$ , and  $1015\text{ cm}^{-1}$  are assigned to the C-H bending vibrations of the benzene rings and the carboxylate groups' vibrations, respectively [31].

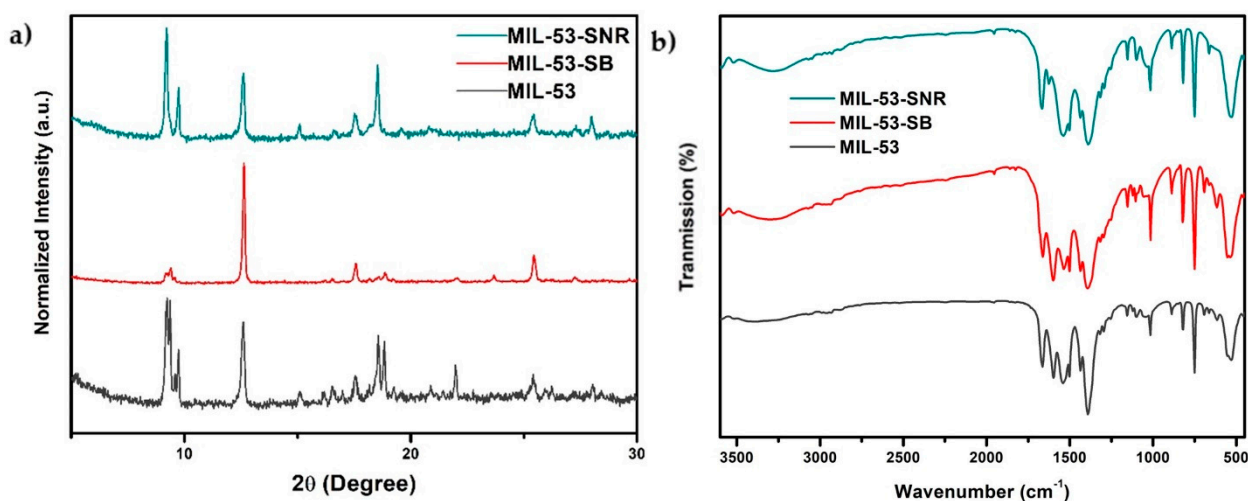


Figure 1. Structural analysis of MIL-53, MIL-53SB, and MIL-53-SNR, (a) XRD pattern, (b) FTIR spectra.

The influence of the sacrificial zinc oxide precursors on the morphology of the samples was further examined by SEM. The SEM micrographs of MIL-53, MIL-53-SB, and MIL-53-SNR are portrayed in Figure 2. The pristine MIL-53, Figure 2a, showed crystalline microrods of approximately 63.5  $\mu\text{m}$  and 7.5  $\mu\text{m}$  in length and width, respectively. These microrods had smooth surfaces and displayed a small amount of debris. Figure 2b represents the micrograph of MIL-53-SB. It is apparent that the MOF particles were less uniform, varying from small microrods to fragments of micro blocks; their texture was slightly rougher with a disordered structure.

In contrast, MIL-53-SNR in Figure 2c displayed fragmented micro shapes with a length of 12.54  $\mu\text{m}$  ( $\pm 2$   $\mu\text{m}$ ) and a width of 4.84  $\mu\text{m}$  ( $\pm 1.3$   $\mu\text{m}$ ), and hardly any microrods were apparent. The surface was extremely rough, and that comes in accordance with its lower XRD diffraction intensities as compared to the ZnO bulk-modified sample. This further indicates the lack of crystallinity in MIL-53-SNR due to the ZnO NRs. For these sacrificial ZnO materials, terephthalic acid is highly likely to bond with the outer surface of the ZnO, severely etching the zinc metal from the ZnO materials and creating MOF-5 layers, similar to previous research with ZIF-8 [39]. This etching process is supposedly continuous until the zinc source is consumed. Nevertheless, MOF-5 does not remain due to the favorable simultaneous process of metal exchange between Zn and Fe, which concurrently creates MIL-53. Therefore, ZnO bulk and ZnO nanorods serve as sacrificial nuclei. Due to their difference in morphology, they exhibit different outcomes. Massive and agglomerated ZnO bulk gets coated and slowly consumed by the 1,4-BDC ligand, serving as nuclei that eventually form MIL-53-SB as fragmented microrods in irregular shapes and sizes instead of the standard MIL-53 microrods. In contrast, ZnO nanorods are thin and well dispersed in the starting solution; thus, they engender more apparent defects as each adjacent nanorod will separately serve as a nuclei for the growth of MIL-53. Assumedly, the closely growing MOFs fuse, forming fragmented microrods with a disordered internal structure, causing the decrease in crystallinity shown in the XRD pattern. Figure 2d shows that Fe-C-SNR maintained the MIL-53-SNR morphology throughout the pyrolysis procedure.

The inductively coupled plasma spectroscopy (ICP) results are presented in Table S1, describing the content of the iron and zinc metal in the as-prepared samples MIL-53-SNR and MIL-53-SB and their pyrolyzed equivalents Fe-C-SNR and Fe-C-SB. Before pyrolysis, both samples showed the expected contents of Fe (21%), matching the reported value of Fe in MIL-53 [38]. In MIL-53-SNR and in MIL-53-SB, the amount of Zn metal detected was extremely low compared to the amount added during the synthesis, which further confirms the sacrificial role of the ZnO in the construction of MIL-53. The zinc metal gets etched to form MOF-5 and gradually diffuses outward of the nuclei during the metal exchange replacement with iron. The relatively higher amount of the ZnO (13 times more) present in

MIL-53-SB than in MIL-53-SNR shows that this process of etching, replacing, and diffusing the Zn is more effective when using thin nanorods than bulk zinc oxide due to their lower concentration of localized zinc.

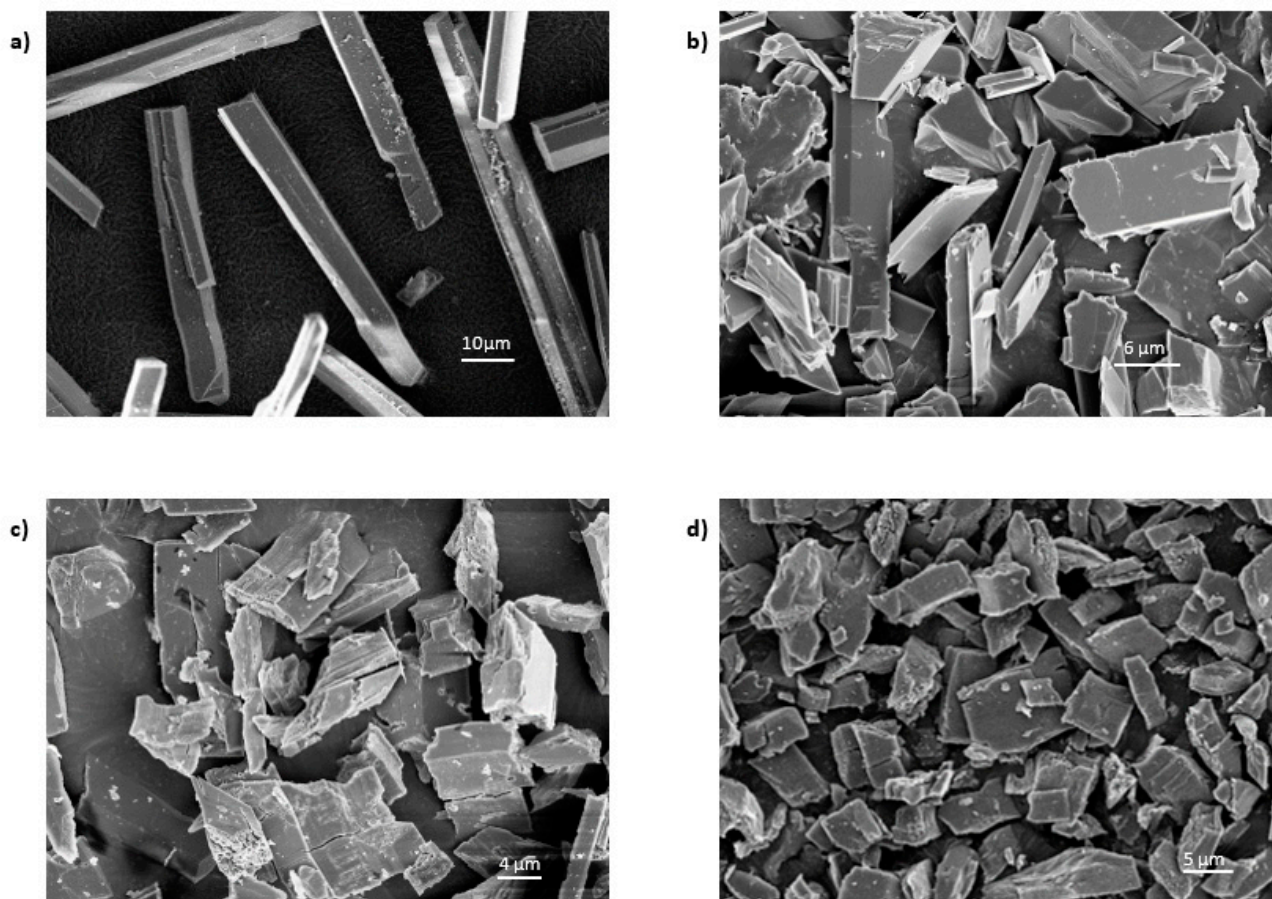


**Figure 2.** SEM micrographs of: (a) MIL-53; (b) MIL-53-SB; (c) MIL-53-SNR; (d) Fe-C-SNR.

The XRD patterns of the pyrolyzed samples, Fe-C, Fe-C-SB, and Fe-C-SNR, are displayed in Figure 3a. The prominent characteristic diffraction peak at  $44.6^\circ$ , present in all three samples, corresponds to the (110) plane of  $\alpha$ -Fe, matching the reported XRDs for ZVI [1]. No other peaks were present, confirming iron is only present as a zero valent. However, Fe-C-SNR displayed a significant decrease in peak width and intensity compared to Fe-C and Fe-C-SB, affirming its smaller particle sizes and less crystalline ZVI phase. The nitrogen adsorption and desorption isotherms, depicted in Figure 3b, were measured to assess the porous structure of the pyrolyzed samples. The BET surface area results for Fe-C, Fe-C-SB, and Fe-C-SNR were  $270 \text{ m}^2 \text{ g}^{-1}$ ,  $220 \text{ m}^2 \text{ g}^{-1}$ , and  $185 \text{ m}^2 \text{ g}^{-1}$ , respectively. The volume and surface area of the micropores and mesopores for Fe-C, Fe-C-SB, and Fe-C-SNR are displayed in Table S2 and Figure 3c. The results for the pore distribution of Fe-C, Fe-C-SB, and Fe-C-SNR displayed normal differences in the microporous region below 5 nm, with Fe-C showing a superior pore volume. On the contrary, in the mesoporous region below 20 nm, Fe-C-SNR showed a remarkable improvement, reaching a volume of  $0.169 \text{ cm}^3 \text{ g}^{-1}$  and a corresponding surface area of  $92 \text{ m}^2 \text{ g}^{-1}$ . This increase in mesopores is linked to the disordered internal structure and the respectively formed defects caused after the pyrolysis of MIL-53-SNR due to the sacrificial zinc oxide nanorods. However, similar progress of the mesopores is not noticeable in Fe-C-SB, as the bulk zinc oxide did not create a similar disordered structure, therefore not favoring the generation of small-scale mesopores. The increase in small mesopores greatly enhanced Fe-C-SNR's MB removal capabilities.

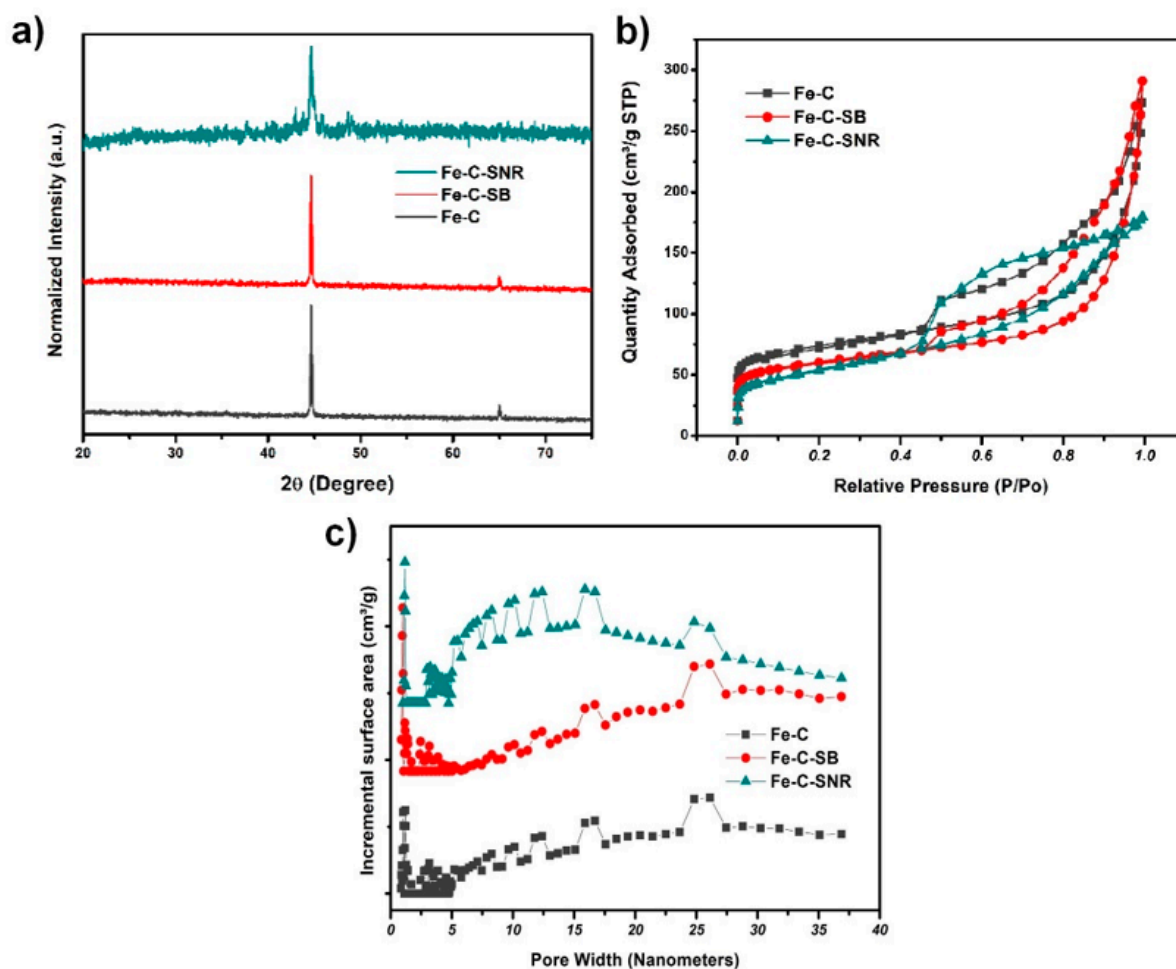


**Figure 3.** Crystallinity and adsorption analysis (a) XRD pattern, (b) N<sub>2</sub> sorption isotherms, (c) pore distribution of Fe-C, Fe-C-SB, Fe-C-SNR.

## 2.2. Adsorption Properties

Fe-C, Fe-C-SB, and Fe-C-SNR were tested as methylene blue adsorbents, and their performances are presented in Figure 4. The UV-absorption patterns are shown in Figure S4. The concentration of the adsorbents used for the experiments was 200 mg L<sup>-1</sup>, and the concentration of the methylene blue solution was 10 mg L<sup>-1</sup>. The times selected were 2, 6, 10, and 30 min. The remaining dye in the solution was measured with UV spectroscopy; thus, the adsorbed MB could be calculated. Fe-C adsorbed 77% of MB after 6 min and reached its maximum adsorption of 85% in 30 min. The addition of the sacrificial ZnO bulk in the synthesis procedure of Fe-C-SB had a negative effect on the removal efficiency, which only reached 63% after 6 min, with a maximum adsorption of 73% after 30 min. This was expected as the N<sub>2</sub> adsorption showed a noticeable decrease in early mesopores due to the use of ZnO bulk.

In contrast, the modification with the sacrificial ZnO nanorods stimulated an excellent improvement in the removal efficiency. Figure 4 displays the astonishing adsorption of 78% in the first 2 min, while after 6 min, a closely total adsorption of 99% was achieved. Further continuing the processing time until 30 min increased the adsorption of MB to full adsorption (100%). Although the surface area of Fe-C-SNR was the lowest of all three samples, the adsorption was greatly enhanced in comparison with Fe-C and Fe-C-SB. This sharp enhancement of MB adsorption was ascribed to the as-confirmed increase in the mesopores, which are superior to micropores for MB adsorption [40,41]. Moreover, due to the smaller particle size of Fe-C-SNR, the pores were easier and accessible faster.

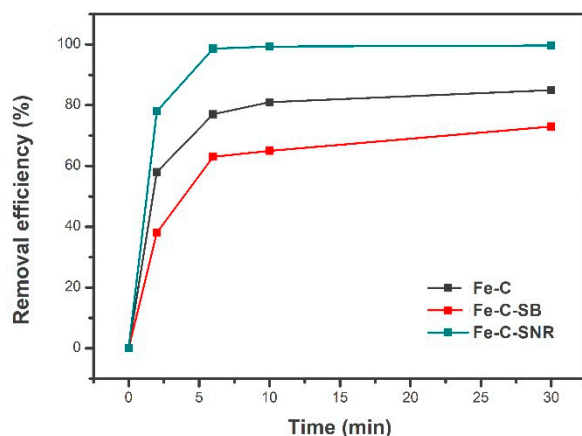


**Figure 4.** Comparison between the removal efficiencies of Fe-C, Fe-C-SB, Fe-C-SNR for methylene blue.

The adsorption kinetics were investigated using pseudo-first-order and pseudo-second-order kinetic models. Respectively, the experimental data were fitted into the Equations (1) and (2):

$$\ln(q_e - q_t) = \ln q_e - k_1 t \quad (1)$$

$$\frac{t}{q_t} = \frac{1}{k_2 q_e^2} + \frac{t}{q_e} \quad (2)$$

where  $q_e$  and  $q_t$  represent the amount of methylene blue adsorbed on the adsorbents at equilibrium, and time  $t$ .  $k_1$  ( $\text{min}^{-1}$ ) and  $k_2$  ( $\text{g mg}^{-1} \text{min}^{-1}$ ) are the rate constants of the first-order and second-order adsorption kinetics. The values of  $q_e$  and  $k_1$  were calculated for the pseudo-first-order model. The values of  $q_e$  and  $k_2$  were calculated for the pseudo-second-order model. Their linear plots are shown in Figure S5, and Table S3 presents the calculated values and the correlation coefficient  $R^2$ . It is seen by the  $R^2 = 0.9997$  that the pseudo-second-order model describes the adsorption kinetics for MB on Fe-C-SNR well.

The effect of the different initial concentrations (10, 20, 40, 60, 80, 100, and 200  $\text{mg L}^{-1}$ ) was evaluated to study the maximum MB adsorption. The set treatment time was 60 min for each sample to ensure the full adsorption of MB onto Fe-C-SNR. The adsorption isotherm is shown in Figure S6. These results are an excellent match for the Langmuir model, which is a widely used model based on the assumption of monolayer adsorption on a homogenous surface. It is represented as follows:

$$= \frac{q_m b C_e}{1 + b C_e}$$

This equation can also be linearized:

$$\frac{C_e}{q_e} = \frac{1}{q_m b} + \frac{C_e}{q_m}$$

where  $C_e$  ( $\text{mg L}^{-1}$ ) represents the equilibrium concentration of MB in the solution,  $Q_e$  and  $Q_m$  ( $\text{mg g}^{-1}$ ) are the adsorption capacity at equilibrium and maximum, respectively, and  $b$  ( $\text{L mg}^{-1}$ ) is the Langmuir constant related to the energy of adsorption. The Langmuir linear adsorption isotherm is shown in Figure 5a.

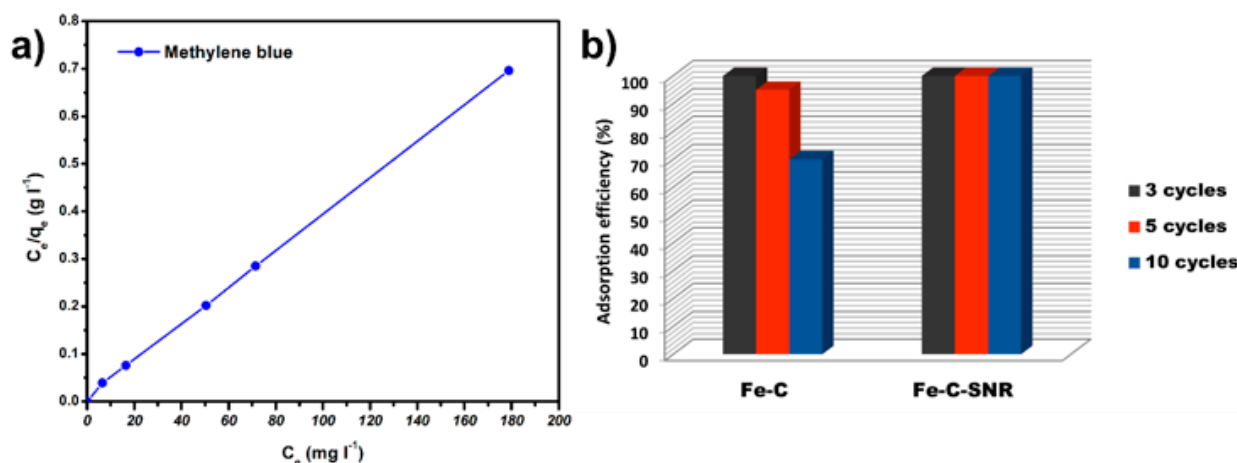


**Figure 5.** (a) Langmuir Linear adsorption isotherm, (b) recyclability of MB adsorption for Fe-C, Fe-C-SNR up to 10 cycles.

Figure 5a displays the linear equation of the Fe-C-SNR correlation coefficient ( $R^2$ ) of 0.9995. Therefore, we can conclude that the adsorption of MB on Fe-C-SNR is a typical monomolecular-layer adsorption. Figure S7 presents the results fitted into the linear equation of the Freundlich model, presenting a correlation coefficient of 0.8479. Following the Langmuir model, the calculated maximum adsorption capacities of Fe-C, Fe-C-SB, and Fe-C-SNR were 125 mg g<sup>-1</sup>, 139 mg g<sup>-1</sup>, and 257 mg g<sup>-1</sup>, respectively. A comparison with other materials reported so far in the literature is available in Table S4. The reuse of an adsorbent is of crucial importance for commercial applications. Furthermore, the methylene blue concentrations that need to be adsorbed in commercial applications are very low. Dependent on the exact location, the permitted methylene blue concentration is as low as 0.2 mg L<sup>-1</sup>. Hence, it is of high importance that the adsorbent can almost entirely adsorb the MB in a solution even at low concentrations. The recyclability of Fe-C-SNR and Fe-C was determined by a series of MB adsorption experiments. The adsorbent (concentration: 1 g L<sup>-1</sup>) was added to a 10 mg L<sup>-1</sup> MB solution, and the treatment time was set to 60 min to reach the equilibrium time for both samples. Afterwards, the dye-adsorbed composites were collected using an external magnet and desorption was performed by using ethanol. Subsequently, the samples were washed with water to remove any adsorbed ethanol. Finally, the adsorbent was reused for up to 10 cycles. The results are presented in Figure 5b. After five cycles, the Fe-C still had a removal efficiency of 94.9%, whereas, after 10 cycles, the efficiency dropped to 70%. The Fe-C-SNR gave an excellent recyclability of 99.8% after five cycles and 99% after 10 cycles. The superior recyclability of Fe-C-SNR in contrast with Fe-C is expected to be due to the already fragmented microrods, which are less likely to be broken during the shaking, desorption, and washing process. To confirm the stability of the material, the XRD pattern before adsorption, with MB adsorbed, and after desorption were measured and are shown in Figure S8. No significant difference was observed, confirming the stability of the material and further confirming the remarkable stability. The highly enhanced maximum adsorption capacity and excellent recyclability makes Fe-SNR a remarkably outstanding adsorbent.

### 3. Materials and Methods

#### 3.1. Methods

All chemicals were purchased from commercial products and used without further purification. Zinc oxide nanorods (ZnO NR) were fabricated by heating zinc acetate (Aladdin Ltd., Shanghai, China) at 300 °C for 12 h in a muffle furnace (TL 1200, Nanjing Bo Yun Tong Instrument Technology Co., Ltd., Nanjing, China). The ZnO NR were cooled and stored for further processing [42]. The MIL-53 (Fe), MIL-53-SNR, and MIL-53-SB were prepared by a solvothermal method. Firstly, 1.4 mmol ZnO NR/ZnO bulk (Sinopharm Chemical Reagent

Co., Ltd., Shanghai, China) were transferred in 20 mL N,N-dimethylformamide (DMF, Sinopharm Chemical Reagent Co., Ltd., Shanghai, China) for MIL-53-SNR and MIL-53-B, respectively. Then, 7 mmol of FeCl<sub>3</sub>·6H<sub>2</sub>O (Aladdin Ltd., Shanghai, China) and 7 mmol of terephthalic acid (BDC, Aladdin Ltd., Shanghai, China) were added to the solution together with 22 mL DMF. The mixture was stirred for 30 min before being transferred into a Teflon-lined autoclave and heated up at 150 °C for 24 h. The formed solid was collected by centrifugation and washed with DMF and ethanol (Sinopharm Chemical Reagent Co., Ltd., Shanghai, China) multiple times. Finally, the samples were dried at 70 °C in a vacuum oven for 24 h. In the second step, F-C, F-C-SNR, and F-C-SB were obtained using a pyrolysis system. Respectively, MIL-53, MIL-53-SNR, and MIL-53-SB (200 mg) were placed in an alumina boat (30 × 60 × 15 mm<sup>3</sup>) and transferred into a quartz tube (OD:60 mm, length: 1000 mm) inside a muffle furnace (TL 1200, Nanjing Bo Yun Tong Instrument Technology Co., Ltd., Nanjing, China) and pyrolyzed at 700 °C with a heating rate of 5 °C min<sup>-1</sup> for 3 h under a flowing Argon atmosphere (50 cm<sup>3</sup> min<sup>-1</sup>) and cooled down naturally.

### 3.2. Characterizations

The material morphology was examined using scanning electron microscopy (FE-SEM, Zeiss Ultra Plus, Oberkochen, Germany). The Powder X-ray diffraction (PXRD) patterns of the samples were recorded on a Rigaku Ultima III diffract meter (Tokyo, Japan) in a wide-angle range ( $2\theta = 3-80^\circ$ ) with Cu-K $\alpha$  ( $\lambda = 0.15406$  nm) 40 kV and 40 mA at a scan speed of 2° min<sup>-1</sup>. The Fourier Transform Infrared Spectroscopy (FTIR) profiles of the samples were measured on a Bruker Tensor 2 apparatus (Ettlingen, Germany) using KBr as reference. The Brunauer–Emmett–Teller (BET) measurements and N<sub>2</sub> adsorption–desorption isotherms were measured with a Porosity Analyzer ASAP 2020 Micromeritics apparatus (Norcross, United States of America) at 77.33 K. The inductively coupled plasma atomic emission spectroscopy (ICP-AES) was performed on an Optima 4300 DV, PerkinElmer Inc., Waltham, United States of America. The pH was measured using a Sartorius PB-10, Göttingen, Germany, at room temperature (25 °C). The UV–Vis absorption spectra were measured with a Shimadzu UV-1800 spectrophotometer, Canby, United States of America, using a quartz cuvette.

### 3.3. Adsorption Experiments

The methylene blue (MB) adsorption experiments were conducted at room temperature (25 °C). In a typical experiment, 2 mg of the adsorbent was brought into 10 mL of 10 mg L<sup>-1</sup> methylene blue solution at its natural pH of 6.2. Then, the mixture was shaken for specific periods. At the required time intervals, a magnet was held next to the mixture to separate the adsorbent from the solution, then 2 mL of a liquid sample was taken, and the dye concentration was determined using spectroscopy by testing the absorbance at  $k_{\max}$  of 664 nm for MB. The MB concentrations were calculated using a calibration curve. The adsorbed MB concentrations were calculated using the initial MB concentration and the MB concentrations after the chosen time intervals. The removal efficiencies at various times were calculated by  $C_t/C_0 \times 100$ , where  $C_t$  presents the adsorbed MB concentration after time  $t$  and  $C_0$  presents the initial MB concentration before adsorption. Blank experiments were also performed, using solutions without any adsorbent, to verify if there was any possible loss due to sorption onto the glass material/syringe surface. The results showed that the sorption onto surfaces was negligible. The adsorption kinetics were also tested using a range of initial MB concentrations ( $C_0$ ) of 10 to 200 mg L<sup>-1</sup>. Furthermore, recyclability tests were performed by the magnetic separation of our adsorbent, then desorption of the adsorbed MB was performed by shaking in 10 mL ethanol twice, subsequently washing the adsorbent with 10 mL water twice, and finally reusing the adsorbent in a new MB solution.

## 4. Conclusions

In summary, we successfully developed a new synthesis procedure to modify MOF-derived materials. Zinc oxide, shaped as nanorods, was added as sacrificial nuclei to form

a modified MIL-53 precursor to synthesize an nZVI-mesoporous carbon nanocomposite. As expected, the nature of the zinc oxide was of crucial importance. The addition of commercial ZnO had no beneficial effect on the adsorption capacity of the pyrolyzed MIL-53. In contrast, sacrificially used zinc oxide nanorods induced mesopores in Fe-C-SNR, directly enhancing the adsorption capacity and recyclability. The maximum adsorption capacity was  $257 \text{ mg g}^{-1}$ , doubling the adsorption of the pyrolyzed MIL-53.

Furthermore, virtually 100% of MB was removed from water using the Fe-C-SNR material (concentration:  $10 \text{ mg L}^{-1}$ ) after 60 min of treatment for 10 consecutive cycles. The zinc oxide nanorods assumedly enhanced the adsorption capability by creating an important number of mesopores, which increased the significant contact area between the ZVI and MB. As the tunability of pore size and the creation of defects in MOFs is of crucial importance, it is foreseen that this synthesis procedure could be beneficial for a wide variety of applications.

**Supplementary Materials:** The following supporting information can be downloaded at: <https://www.mdpi.com/article/10.3390/inorganics10050059/s1>, Figure S1: SEM micrograph of zinc oxide nanorods; Figure S2: X-ray diffraction pattern of zinc oxide nanorods; Figure S3: X-ray diffraction patterns of MIL-53-SNR, MIL-53-SB, MIL-53; Table S1: ICP results of MIL-53-SB and MIL-53-SNR; Table S2: Volume and surface area of micropores and mesopores of pyrolyzed samples; Figure S4: Adsorption performance of the three samples: (a) Fe-C, (b) Fe-C-SB, (c) Fe-C-SNR; Table S3: Kinetic parameters of pseudo first order and pseudo second order models for the adsorption of methylene blue onto Fe-C-SNR; Figure S5: Kinetic plots for the adsorption of methylene blue on Fe-C-SNR, (a) Plot of the pseudo first order kinetic model, (b) plot of the pseudo second order kinetic model; Figure S6: Adsorption isotherm of methylene blue on Fe-C-SNR; Figure S7: Freundlich Linear adsorption isotherm; Table S4 [1,38,43–49]: Comparative table of the maximum adsorbed methylene blue from literature; Figure S8: X-ray diffraction pattern of Fe-C-SNR before adsorption, with MB adsorbed, and after desorption

**Author Contributions:** S.D.: conceptualization, investigation, writing—original draft preparation; M.E.H.: conceptualization, investigation, writing—original draft preparation; S.C.: investigation, methodology; S.Z.: validation, writing—review and editing; F.V.: supervision, funding acquisition, writing—review and editing. All authors have read and agreed to the published version of the manuscript.

**Funding:** This research was funded by the National Natural Science Foundation of China (Contract number 21172027), and the Chinese Scholarship Council (CSC No. 2017GXZ006032).

**Institutional Review Board Statement:** Not applicable.

**Informed Consent Statement:** Not applicable.

**Conflicts of Interest:** The authors declare no conflict of interest. The funders had no role in the design of the study; in the collection, analyses, or interpretation of data; in the writing of the manuscript; or in the decision to publish the results.

## References

1. Liu, J.; Wang, Y.; Fang, Y.; Mwamulima, T.; Song, S.; Peng, C. Removal of Crystal Violet and Methylene Blue from Aqueous Solutions Using the Fly Ash-Based Adsorbent Material-Supported Zero-Valent Iron. *J. Mol. Liq.* **2018**, *250*, 468–476. [CrossRef]
2. Ahmad, A.; Rafatullah, M.; Sulaiman, O.; Ibrahim, M.H.; Hashim, R. Scavenging Behaviour of Meranti Sawdust in the Removal of Methylene Blue from Aqueous Solution. *J. Hazard. Mater.* **2009**, *170*, 357–365. [CrossRef] [PubMed]
3. Katheresan, V.; Kansedo, J.; Lau, S.Y. Journal of Environmental Chemical Engineering. *J. Environ. Chem. Eng.* **2018**, *6*, 4676–4697. [CrossRef]
4. Dang, T.-D.; Le, H.T.T.; Nguyen, D.A.; Duc, D.; Dinh, L.; Nguyen, D. A Magnetic Hierarchical Zero-Valent Iron Nanoflake-Decorated Graphene Nanoplate Composite for Simultaneous Adsorption and Reductive Degradation of Rhodamine B. *New J. Chem.* **2020**, *44*, 9083. [CrossRef]
5. Fan, Y.; Ida, S.; Staykov, A.; Akbay, T.; Hagiwara, H.; Matsuda, J.; Kaneko, K.; Ishihara, T. Ni-Fe Nitride Nanoplates on Nitrogen-Doped Graphene as a Synergistic Catalyst for Reversible Oxygen Evolution Reaction and Rechargeable Zn-Air Battery. *Small* **2017**, *13*, 1700099. [CrossRef] [PubMed]

6. Shao, Y.; Gao, Y.; Yue, Q.; Kong, W.; Gao, B.; Wang, W.; Jiang, W. Degradation of Chlortetracycline with Simultaneous Removal of Copper (II) from Aqueous Solution Using Wheat Straw-Supported Nanoscale Zero-Valent Iron. *Chem. Eng. J.* **2020**, *379*, 122384. [[CrossRef](#)]
7. Zhang, S.; Zhao, Y.; Yang, K.; Liu, W.; Xu, Y.; Liang, P.; Zhang, X.; Huang, X. Versatile Zero Valent Iron Applied in Anaerobic Membrane Reactor for Treating Municipal Wastewater: Performances and Mechanisms. *Chem. Eng. J.* **2020**, *382*, 123000. [[CrossRef](#)]
8. Sun, Y.; Li, J.; Huang, T.; Guan, X. The Influences of Iron Characteristics, Operating Conditions and Solution Chemistry on Contaminants Removal by Zero-Valent Iron: A Review. *Water Res.* **2016**, *100*, 277–295. [[CrossRef](#)]
9. Fu, F.; Dionysiou, D.D.; Liu, H. The Use of Zero-Valent Iron for Groundwater Remediation and Wastewater Treatment: A Review. *J. Hazard. Mater.* **2014**, *267*, 194–205. [[CrossRef](#)]
10. Shaibu, S.E.; Adekola, F.A.; Adegoke, H.I.; Ayanda, O.S. A Comparative Study of the Adsorption of Methylene Blue onto Synthesized Nanoscale Zero-Valent Iron-Bamboo and Manganese-Bamboo Composites. *Materials* **2014**, *7*, 4493–4507. [[CrossRef](#)]
11. Ezzatahmedi, N.; Ayoko, G.A.; Millar, G.J.; Speight, R.; Yan, C.; Li, J.; Li, S.; Zhu, J.; Xi, Y. Clay-Supported Nanoscale Zero-Valent Iron Composite Materials for the Remediation of Contaminated Aqueous Solutions: A Review. *Chem. Eng. J.* **2017**, *312*, 336–350. [[CrossRef](#)]
12. Woo, H.; Park, J.; Lee, S.; Lee, S. Effects of Washing Solution and Drying Condition on Reactivity of Nano-Scale Zero Valent Irons (NZVIs) Synthesized by Borohydride Reduction. *Chemosphere* **2014**, *97*, 146–152. [[CrossRef](#)] [[PubMed](#)]
13. Teng, W.; Fan, J.; Wang, W.; Bai, N.; Liu, R.; Liu, Y.; Deng, Y.; Kong, B.; Yang, J.; Zhao, D.; et al. Nanoscale Zero-Valent Iron in Mesoporous Carbon (NZVI@C): Stable Nanoparticles for Metal Extraction and Catalysis. *J. Mater. Chem. A* **2017**, *5*, 4478–4485. [[CrossRef](#)]
14. Bao, T.; Dامتie, M.M.; Hosseinzadeh, A.; Wei, W.; Jin, J.; Phong Vo, H.N.; Ye, J.S.; Liu, Y.; Wang, X.F.; Yu, Z.M.; et al. Bentonite-Supported Nano Zero-Valent Iron Composite as a Green Catalyst for Bisphenol A Degradation: Preparation, Performance, and Mechanism of Action. *J. Environ. Manag.* **2020**, *260*, 110105. [[CrossRef](#)] [[PubMed](#)]
15. Liu, T.; Wang, Z.L.; Zhao, L.; Yang, X. Enhanced Chitosan/Fe<sup>0</sup>-Nanoparticles Beads for Hexavalent Chromium Removal from Wastewater. *Chem. Eng. J.* **2012**, *189–190*, 196–202. [[CrossRef](#)]
16. Sun, Z.; Zheng, S.; Ayoko, G.A.; Frost, R.L.; Xi, Y. Degradation of Simazine from Aqueous Solutions by Diatomite-Supported Nanosized Zero-Valent Iron Composite Materials. *J. Hazard. Mater.* **2013**, *263*, 768–777. [[CrossRef](#)]
17. Wang, J.; Liu, G.; Li, T.; Zhou, C.; Qi, C. Zero-Valent Iron Nanoparticles (NZVI) Supported by Kaolinite for CuII and NiII Ion Removal by Adsorption: Kinetics, Thermodynamics, and Mechanism. *Aust. J. Chem.* **2015**, *68*, 1305. [[CrossRef](#)]
18. Mystrioti, C.; Sparis, D.; Papasiopi, N.; Xenidis, A.; Dermatas, D.; Chrysochoou, M. Assessment of Polyphenol Coated Nano Zero Valent Iron for Hexavalent Chromium Removal from Contaminated Waters. *Bull. Environ. Contam. Toxicol.* **2015**, *94*, 302–307. [[CrossRef](#)]
19. Shu, H.Y.; Chang, M.C.; Chen, C.C.; Chen, P.E. Using Resin Supported Nano Zero-Valent Iron Particles for Decoloration of Acid Blue 113 Azo Dye Solution. *J. Hazard. Mater.* **2010**, *184*, 499–505. [[CrossRef](#)]
20. Fu, R.; Yang, Y.; Xu, Z.; Zhang, X.; Guo, X.; Bi, D. The Removal of Chromium (VI) and Lead (II) from Groundwater Using Sepiolite-Supported Nanoscale Zero-Valent Iron (S-NZVI). *Chemosphere* **2015**, *138*, 726–734. [[CrossRef](#)]
21. Mortazavian, S.; An, H.; Chun, D.; Moon, J. Activated Carbon Impregnated by Zero-Valent Iron Nanoparticles (AC/NZVI) Optimized for Simultaneous Adsorption and Reduction of Aqueous Hexavalent Chromium: Material Characterizations and Kinetic Studies. *Chem. Eng. J.* **2018**, *353*, 781–795. [[CrossRef](#)]
22. Li, J.; Zhou, Q.; Liu, Y.; Lei, M. Recyclable Nanoscale Zero-Valent Iron-Based Magnetic Polydopamine Coated Nanomaterials for the Adsorption and Removal of Phenanthrene and Anthracene. *Sci. Technol. Adv. Mater.* **2017**, *18*, 3–16. [[CrossRef](#)]
23. Tristão, J.C.; de Mendonça, F.G.; Lago, R.M.; Ardisson, J.D. Controlled Formation of Reactive Fe Particles Dispersed in a Carbon Matrix Active for the Oxidation of Aqueous Contaminants with H<sub>2</sub>O<sub>2</sub>. *Environ. Sci. Pollut. Res.* **2015**, *22*, 856–863. [[CrossRef](#)]
24. Van Tran, T.; Bui, Q.T.P.; Nguyen, T.D.; Thanh Ho, V.T.; Bach, L.G. Application of Response Surface Methodology to Optimize the Fabrication of ZnCl<sub>2</sub>-Activated Carbon from Sugarcane Bagasse for the Removal of Cu<sup>2+</sup>. *Water Sci. Technol.* **2017**, *75*, 2047–2055. [[CrossRef](#)]
25. Van Thuan, T.; Quynh, B.T.P.; Nguyen, T.D.; Ho, V.T.T.; Bach, L.G. Response Surface Methodology Approach for Optimization of Cu<sup>2+</sup>, Ni<sup>2+</sup> and Pb<sup>2+</sup> Adsorption Using KOH-Activated Carbon from Banana Peel. *Surf. Interfaces* **2017**, *6*, 209–217. [[CrossRef](#)]
26. Shi, X.; Ruan, W.; Hu, J.; Fan, M.; Cao, R.; Wei, X. Optimizing the Removal of Rhodamine B in Aqueous Solutions by Reduced Graphene Oxide-Supported Nanoscale Zerovalent Iron (NZVI/RGO) Using an Artificial Neural Network-Genetic Algorithm (ANN-GA). *Nanomaterials* **2017**, *7*, 134. [[CrossRef](#)]
27. Stefaniuk, M.; Oleszczuk, P.; Ok, Y.S. Review on Nano Zerovalent Iron (NZVI): From Synthesis to Environmental Applications. *Chem. Eng. J.* **2016**, *287*, 618–632. [[CrossRef](#)]
28. Wang, Z.; Yang, J.; Li, Y.; Zhuang, Q.; Gu, J. In Situ Carbothermal Synthesis of Nanoscale Zero-Valent Iron Functionalized Porous Carbon from Metal-Organic Frameworks for Efficient Detoxification of Chromium(VI). *Eur. J. Inorg. Chem.* **2018**, *2018*, 23–30. [[CrossRef](#)]
29. Zan, J.; Song, H.; Zuo, S.; Chen, X.; Xia, D.; Li, D. MIL-53(Fe)-Derived Fe<sub>2</sub>O<sub>3</sub> with Oxygen Vacancy as Fenton-like Photocatalysts for the Elimination of Toxic Organics in Wastewater. *J. Clean. Prod.* **2020**, *246*, 118971. [[CrossRef](#)]

30. Liang, R.; Jing, F.; Shen, L.; Qin, N.; Wu, L. MIL-53(Fe) as a Highly Efficient Bifunctional Photocatalyst for the Simultaneous Reduction of Cr(VI) and Oxidation of Dyes. *J. Hazard. Mater.* **2015**, *287*, 364–372. [[CrossRef](#)]
31. Vu, T.A.; Le, G.H.; Dao, C.D.; Dang, L.Q.; Nguyen, K.T.; Nguyen, Q.K.; Dang, P.T.; Tran, H.T.K.; Duong, Q.T.; Nguyen, T.V.; et al. Arsenic Removal from Aqueous Solutions by Adsorption Using Novel MIL-53(Fe) as a Highly Efficient Adsorbent. *RSC Adv.* **2015**, *5*, 5261–5268. [[CrossRef](#)]
32. Serre, C.; Millange, F.; Thouvenot, C.; Noguès, M.; Marsolier, G.; Louër, D.; Férey, G. Very Large Breathing Effect in the First Nanoporous Chromium(III)-Based Solids: MIL-53 or CrIII(OH)·{O2C-C6H4-CO2}·{HO2C-C6H4-CO2H}x·H2Oy. *J. Am. Chem. Soc.* **2002**, *124*, 13519–13526. [[CrossRef](#)] [[PubMed](#)]
33. Cho, W.; Park, S.; Oh, M. Coordination Polymer Nanorods of Fe-MIL-88B and Their Utilization for Selective Preparation of Hematite and Magnetite Nanorods. *Chem. Commun.* **2011**, *47*, 4138–4140. [[CrossRef](#)] [[PubMed](#)]
34. Scherb, C.; Schödel, A.; Bein, T. Metal-Organic Frameworks Directing the Structure of Metal-Organic Frameworks by Oriented Surface Growth on an Organic Monolayer. *Angew. Chem. Int. Ed.* **2008**, *47*, 5777–5779. [[CrossRef](#)]
35. Pham, H.; Ramos, K.; Sua, A.; Acuna, J.; Slowinska, K.; Nguyen, T.; Bui, A.; Weber, M.D.R.; Tian, F. Tuning Crystal Structures of Iron-Based Metal–Organic Frameworks for Drug Delivery Applications. *ACS Omega* **2020**, *5*, 3418–3427. [[CrossRef](#)]
36. Cai, X.; Lin, J.; Pang, M. Facile Synthesis of Highly Uniform Fe-MIL-88B Particles. *Cryst. Growth Des.* **2016**, *16*, 3565–3568. [[CrossRef](#)]
37. Naeimi, S.; Faghihian, H. Application of Novel Metal Organic Framework, MIL-53(Fe) and Its Magnetic Hybrid: For Removal of Pharmaceutical Pollutant, Doxycycline from Aqueous Solutions. *Environ. Toxicol. Pharmacol.* **2017**, *53*, 121–132. [[CrossRef](#)]
38. Banerjee, A.; Gokhale, R.; Bhatnagar, S.; Jog, J.; Bhardwaj, M.; Lefez, B.; Hannoyer, B.; Ogale, S. MOF Derived Porous Carbon-Fe<sub>3</sub>O<sub>4</sub> Nanocomposite as a High Performance, Recyclable Environmental Superadsorbent. *J. Mater. Chem.* **2012**, *22*, 19694–19699. [[CrossRef](#)]
39. Stassen, I.; Campagnol, N.; Fransaer, J.; Vereecken, P.; De Vos, D.; Ameloot, R. Solvent-Free Synthesis of Supported ZIF-8 Films and Patterns through Transformation of Deposited Zinc Oxide Precursors. *CrystEngComm* **2013**, *15*, 9308–9311. [[CrossRef](#)]
40. Cao, X.; Wang, R.; Peng, Q.; Zhao, H.; Fan, H.; Liu, H.; Liu, Q. Effect of Pore Structure on the Adsorption Capacities to Different Sizes of Adsorbates by Ferrocene-Based Conjugated Microporous Polymers. *Polymer* **2021**, *233*, 124192. [[CrossRef](#)]
41. Yuan, X.; Zhuo, S.P.; Xing, W.; Cui, H.Y.; Dai, X.D.; Liu, X.M.; Yan, Z.F. Aqueous Dye Adsorption on Ordered Mesoporous Carbons. *J. Colloid Interface Sci.* **2007**, *310*, 83–89. [[CrossRef](#)] [[PubMed](#)]
42. Horzum, N.; Hilal, M.E.; Isik, T. Enhanced Bactericidal and Photocatalytic Activities of ZnO Nanostructures by Changing the Cooling Route. *New J. Chem.* **2018**, *42*, 11831–11838. [[CrossRef](#)]
43. Frost, R.L.; Xi, Y.; He, H. Synthesis, Characterization of Palygorskite Supported Zero-Valent Iron and Its Application for Methylene Blue Adsorption. *J. Colloid Interface Sci.* **2010**, *341*, 153–161. [[CrossRef](#)]
44. Shi, Z.; Wang, Y.; Sun, S.; Zhang, C.; Wang, H. Removal of Methylene Blue from Aqueous Solution Using Mg-Fe, Zn-Fe, Mn-Fe Layered Double Hydroxide. *Water Sci. Technol.* **2020**, *81*, 2522–2532. [[CrossRef](#)]
45. Hamdy, A.; Hamdy, M.K.; Nasr, M. Zero-Valent Iron Nanoparticles for Methylene Blue Removal from Aqueous Solutions and Textile Wastewater Treatment, with Cost Estimation. *Water Sci. Technol.* **2018**. [[CrossRef](#)]
46. Zhou, Y.; Gao, B.; Zimmerman, A.R.; Chen, H.; Zhang, M.; Cao, X. Biochar-Supported Zerovalent Iron for Removal of Various Contaminants from Aqueous Solutions. *Bioresour. Technol.* **2014**, *152*, 538–542. [[CrossRef](#)]
47. Arabi, S.; Sohrabi, M.R. Removal of Methylene Blue, a Basic Dye, from Aqueous Solutions Using Nano-Zerovalent Iron. *Water Sci. Technol.* **2014**, *70*, 24–31. [[CrossRef](#)]
48. Aslam, S.; Zeng, J.; Subhan, F.; Li, M.; Lyu, F.; Li, Y.; Yan, Z.; Aslam, S.; Zeng, J.; Subhan, F.; et al. Accepted Manuscript In Situ One-Step Synthesis of Fe<sub>3</sub>O<sub>4</sub> @MIL-100(Fe) Core-Shells for Adsorption of Methylene Blue from Water In Situ One-Step Synthesis of Fe<sub>3</sub>O<sub>4</sub> @MIL-100(Fe) Core-Shells for Adsorption of Methylene Blue from Water. *J. Colloid Interface Sci.* **2017**. [[CrossRef](#)]
49. Wu, R.; Liu, L.-H.; Zhao, L.; Zhang, X.; Xie, J.; Yu, B.; Ma, X.; Yang, S.-T.; Wang, H.; Liu, Y. Hydrothermal Preparation of Magnetic Fe<sub>3</sub>O<sub>4</sub> @C Nanoparticles for Dye Adsorption. *Biochem. Pharmacol.* **2014**, *2*, 907–913. [[CrossRef](#)]